| | |
|---|---|
| ***Title*** | Long-circulating magnetoliposomes as surrogates for assessing pancreatic tumour permeability and nanoparticle deposition |
| ***Authors(s)*** | Moloney, Cara, Chaudhuri, Tista Roy, Spernyak, Joseph A., Straubinger, Robert M., Brougham, Dermot F. |
| ***Publication date*** | 2023-03-01 |
| ***Publication information*** | Moloney, Cara, Tista Roy Chaudhuri, Joseph A. Spernyak, Robert M. Straubinger, and Dermot F. Brougham. "Long-Circulating Magnetoliposomes as Surrogates for Assessing Pancreatic Tumour Permeability and Nanoparticle Deposition." Elsevier, March 1, 2023. https://doi.org/10.1016/j.actbio.2022.12.057. |
| ***Publisher*** | Elsevier |
| ***Item record/more information*** | http://hdl.handle.net/10197/25536 |
| ***Publisher's version (DOI)*** | 10.1016/j.actbio.2022.12.057 |

# Long-circulating magnetoliposomes as surrogates for assessing pancreatic tumour permeability and nanoparticle deposition

Cara Moloney [a†‡], Tista Roy Chaudhuri [b], Joseph A. Spernyak [c], Robert M. Straubinger *[b,c], Dermot F. Brougham*[a]

[a] School of Chemistry, University College Dublin, Belfield, Dublin 4, Ireland

[b] Dept. of Pharmaceutical Sciences, School of Pharmacy and Pharmaceutical Sciences,
University at Buffalo, State University of New York, Buffalo, NY, 14214, USA

[c] Department of Cell Stress Biology
Roswell Park Comprehensive Cancer Center, Buffalo, NY 14263

[†] **1st author**

[*] **Corresponding author**

**KEYWORDS:** liposomes, magnetic nanoparticles, MRI tracking, pancreatic cancer

## ABSTRACT

Nanocarriers are candidates for cancer chemotherapy delivery, with growing numbers of clinically-approved nano-liposomal formulations such as Doxil® and Onivyde® (liposomal doxorubicin and irinotecan) providing proof-of-concept. However, their complex biodistribution and the varying susceptibility of individual patient tumours to nanoparticle deposition remains a clinical challenge. Here we describe the preparation, characterisation, and biological evaluation of phospholipidic structures containing solid magnetic cores (SMLs) as an MRI-trackable surrogate that could aid in the clinical development and deployment of nano-liposomal formulations. Through the sequential assembly of size-defined iron oxide nanoparticle clusters with a stabilizing anionic phospholipid inner monolayer and an outer monolayer of independently-selectable composition, SMLs can mimic physiologically a wide range of nano-liposomal carrier compositions. In patient-derived xenograft models of pancreatic adenocarcinoma, similar tumour deposition of SML and their nano-liposomal counterparts of identical bilayer composition was observed *in vivo*, both at the tissue level (fluorescence intensities of $1.5 \times 10^8 \pm 1.8 \times 10^7$ and $1.2 \times 10^8 \pm 6.3 \times 10^7$, respectively; ns, 99% confidence interval) and non-invasively using MR imaging. We observed superior capabilities of SML as a surrogate for nano-liposomal formulations as compared to other clinically-approved iron oxide nano-formulations (ferumoxytol). In combination with diagnostic and therapeutic imaging tools, SMLs have high clinical translational potential to predict nano-liposomal drug carrier deposition and could assist in stratifying patients into treatment regimens that promote optimal tumour deposition of nanoparticulate chemotherapy carriers.

## 1. INTRODUCTION

Liposomes have broad applications in drug delivery and remain at the forefront of drug carrier research because of their compositional diversity and physicochemical properties, biocompatibility, and low immunogenicity[1-4]. Among the nanoparticulate formulations that have advanced to clinical evaluation, liposome-based formulations represent a substantial majority of those approved for clinical use[5]. Liposomes can modulate pharmacokinetics (PK) and pharmacological response profiles (pharmacodynamics; PD) of the encapsulated drugs and allow for enhanced and site-specific drug delivery[6-8]. Their composition can be modified to optimise outcomes by controlling their outer surface- and membrane bilayer properties. For example, the inclusion of sterically-stabilizing PEGylated lipids in the membrane produces long-circulating, sterically-stabilised liposomes (SSL), which have reduced bio-recognition and clearance mechanisms *in vivo*[9]. The emergence of patient-derived biomaterials such as exosome delivery systems, which can provide truly personalised cancer treatments with dramatically reduced immunogenicity and clearance *in vivo*[10, 11], and the fact that lipid composition can also control carrier drug release rates to provide sustained-release capabilities, demonstrates the potential of lipid-stabilised platform nano-systems for imaging and delivery.

The growing number of FDA-approved liposomal formulations for drug delivery include Doxil®, an SSL formulation containing doxorubicin for breast, ovarian, and other cancers, and Onivyde®, an SSL formulation containing irinotecan, which received fast-track approval for pancreatic cancer[12-15]. These SSL formulations share similar compositions, with a high phase-transition phosphatidylcholine (PC; hydrogenated soy PC or distearoyl-PC) as the majority phospholipid, a high cholesterol content, and a minority phospholipid component anchoring the polyethyleneglycol (PEG) steric-stabilizing polymer coat (1,2-distearoyl-sn-glycero-3-phosphoethanolamine-N-[PEG-2000]; DSPE-PEG-2000). However, inter-individual variability in patient tumour uptake of SSL has been reported, and the magnitude of uptake correlates with clinical efficacy of the encapsulated drug[16], suggesting the need to identify those patients most likely to benefit from nanoparticle-based therapies, even for established formulations such as Doxil®. Furthermore, 'tumour priming' strategies are recognised for their potential to compromise *in vivo* drug delivery barriers and increase drug, antibody, and nanoliposome delivery to low perfusion/permeability cancers, but clinical development of these strategies has been challenging[17-19].

Magnetoliposomes (MLs), comprised of liposomes encapsulating magnetic nanoparticles (MNPs), were first prepared by De Cuyper et al in the 1980s[20], and offer a means of addressing this challenge. Most approaches to preparations involve thin film rehydration using MNP suspensions, producing cores of densely packed MNPs within an aqueous lumen[21]. We have developed solid magnetoliposomes (SMLs) as MRI-trackable surrogates for non-invasive tracking of liposome deposition and potentially that of other lipidic nanocarriers. SMLs have a solid core comprised of clusters of small, primary iron oxide MNPs that provide contrast-generating potential for MRI, which are encapsulated within a lipid bilayer of tuneable composition that provides a liposome-mimetic outer surface. The absence of a lumen may aid with colloidal stability and retention of size in blood following administration. By combining both liposomal and magnetic characteristics, we envisage their utility as MRI-trackable surrogates for predicting individual patient tumour nanoparticle deposition/response and as a platform for additional potential functions, including magnetic (static field gradient) targeting and hyperthermic drug delivery capabilities with AC-magnetic field excitation[22-24].

First-generation SMLs were prepared by alkaline coprecipitation of iron salts in the presence of phospholipids[25]. However, their magnetic and magnetic resonance (MR) properties were moderate, thus limiting *in vivo* applications. Here we developed a two-step synthesis process employing (1) surfactant-free thermal-decomposition[26], which enables us to define the primary MNP size, and thereby prepare SMLs having a reproducible MNP cluster size, improved monodispersity, MNP crystallinity, and hence MR properties, followed by (2) sequential chemisorption of an inner phospholipid monolayer that interacts tightly with the exposed iron oxide surface of the MNP clusters, and then physisorption of an outer phospholipid layer, resulting in a phase transfer of the final constructs. This approach enables tuning of surface characteristics to produce a library of stable SML suspensions of diverse physicochemical characteristics, incorporating (i) PEGylated lipids for improving circulation time, (ii) dyes for *in vivo* optical imaging, and (iii) lipidic anchors for surface-conjugation of targeting ligands. Notably, inclusion of DSPE-PEG-2000 in the outer phospholipid leaflet produces SML-PEG that mimics the surface composition of long-circulating SSL drug carriers such as Doxil® and Onivyde®

A primary motivation in developing the SML system was to address challenges of pancreatic adenocarcinoma (PDAC), which is currently the 3rd-leading cause of cancer death in the western world and projected to rise to 2nd in the near future[27-29]. With 7-9% survival, the lethality of PDAC results from its advanced stage at diagnosis, the rapid progression of the disease, and the minimal benefits of conventional chemotherapy[30-33]. The desmoplastic stromal reaction in PDAC, which results in amplification of the stromal mass and exceedingly low functional tumour microvessel density, unquestionably contributes to treatment resistance, and the poor selectivity of chemotherapy elevates toxicity[17, 34, 35]. Strategies to meet these challenges include therapeutic compromise of the drug delivery barrier established by the desmoplastic reaction, in order to increase nanoparticulate drug delivery, and treatment stratification for individual patients to enhance the likelihood of their response to nanoparticulate formulations. Without prior stratification, patients whose tumours are low in susceptibility to nanoparticle deposition would experience the toxicity of therapy without reasonable benefit of efficacy. Thus, we hypothesized that by optimal engineering of SML formulation, they could be applied as a non-invasive MR-imaging stratification tool to identify individuals in whom high levels of liposomal Doxil$^{®}$ or Onivyde$^{®}$ deposition could be achieved.

To evaluate this possibility, the MRI capabilities and tumour deposition of SML-PEG were evaluated *in vitro* and *in vivo* for a range of PDAC models. The SML-PEG MRI responses were benchmarked against ferumoxytol (FMX), a commonly-investigated $T_2$ contrast agent in preclinical MRI[36, 37], which was clinically approved for treatment for anaemia in adults having chronic kidney disease[38] but withdrawn from use in the UK and EU over safety concerns[39]. The resultant SMLs enable different imaging modalities, have high clinical translational potential for predicting tumour nanoparticle deposition under both unperturbed conditions and in conjunction with stroma-modulating pre-treatment strategies.

## 2. MATERIALS AND METHODS

### 2.1 Materials

Iron (III) acetylacetonate (≥99.9%; $Fe(acac)_3$), 1,2-dioleoyl-sn-glycero-3-phospho-rac-(1-glycerol) sodium salt (≥98.0%; DOPG), benzyl alcohol (ACS reagent, ≥99.0%), phosphate buffered saline (PBS) tablets, methanol (ACS reagent, ≥99.8%; MeOH), acetone (CHROMASOLV® ≥99.8%), methyl cellulose and TWEEN® 80 were purchased from Sigma-Aldrich. 1,2-distearoyl-sn-glycero-3-phosphocholine (DSPC), 1,2-distearoyl-sn-glycero-3-phosphoethanolamine-N-[amino (polyethylene glycol)-2000] (DSPE-PEG-2000 amine), 1,2-dioleoyl-sn-glycero-3-phosphocholine (DOPC) and cholesterol were purchased from Avanti Polar Lipids Inc.. 1,1'-dioctadecyl-3,3,3',3'-tetramethylindodicarbocyanine 4-chlorobenzenesulfonate Salt (DiD-DS), 1,1’-Dioctadecyl-3,3,3’,3’-Tetramethylindocarbocyanine-5,5’-Disulfonic Acid (DiR-DS), chloroform (Reagent grade; $CHCl_3$), ammonia (35%; $NH_4OH$), Prolong™ Gold Antifade mounting medium with DAPI

(4′,6-diamidino-2-phenylindole), ethanol (absolute), xylene, Permount™ mounting media, and microscope slides (TruBond 380 Blue) were purchased from ThermoFisher. The SMO-inhibitor of sonic hedgehog signalling (sHHi), NVP-LDE225 was purchased from ChemieTek (Indianapolis, IA). FMX was purchased from AMAG Pharmaceuticals, USA. All chemicals were used without further purification. De-ionised water was obtained from a Millipore Milli Q Gradient system fitted with a 0.22 µm Millipak Express 20 filter and had a resistivity of <18.2 MΩ.cm.

### 2.2 Preparation of Primary Magnetic Nanoparticles

A surfactant-free decomposition method was chosen for MNP preparation so that the phospholipids could be chemisorbed to the MNP surface without prior ligand exchange, and to enhance the magnetic properties as compared to MNPs prepared by co-precipitation methods. Primary MNPs of 8.6 and 12.4 nm were prepared by methods previously reported[40], which was derived from the Pinna method[26]. In brief, 20 mL of 141.6 mM $Fe(acac)_3$ in benzyl alcohol was purged with $N_2$ for 20 minutes and refluxed at 205 °C for 7 hours. The resulting black solution contained 10 mg/ml $\gamma$-$Fe_2O_3$ (*c.* 90% yield) of 8.6 nm MNPs as determined by TEM (Figure S1). To prepare larger MNPs, 20 mL of 8.6 nm MNPs were washed twice with benzyl alcohol and resuspended in 20 mL of 141.6 mM $Fe(acac)_3$ in benzyl alcohol. The solution was purged with $N_2$ for 20 minutes and refluxed at 205 °C for 7 hours. The resulting black solution contained 20 mg/mL $\gamma$-$Fe_2O_3$ (*c.* 90% yield) of 12.4 nm MNPs (Figure S1). MNPs were stored at room temperature under $N_2$ until use. MNPs prepared using the original method were reported as comprising the magnetite ($Fe_3O_4$) phase. Using our modification, the resulting MNPs were composed predominantly of maghemite ($\gamma$-$Fe_2O_3$), as confirmed by X-ray adsorption spectroscopy (XAS) analysis[41].

### 2.3 Preparation of Solid Magnetic Liposomes

The general method for SML preparation derives from our previous approach[25], but is now divided into two steps: step one leads to the formation of an inner phospholipid monolayer on the MNP surface (mono-SML), and step two completes the phospholipid bilayer by addition of a second, external membrane leaflet, thus allowing for independent control of the bilayer leaflet composition. The quantity of phospholipid required to prepare a monodisperse, stable aqueous SML suspension is dependent upon the size and number of primary MNPs. It was found that in the first step, SMLs prepared with 0.88 surface equivalents (SE) of phospholipid formed stable, monodisperse suspensions. A SE of 1.0 is the theoretical amount required to form a complete phospholipid monolayer coating on all the MNPs present, assuming they were fully dispersed; Table S1 provides details of this calculation. Above and below this optimum SE coverage, larger, unstable aggregates formed. Table 1 reports the optimum phospholipid content required to form SMLs from 5 mL of 8.6 and 12.4 nm MNPs (10 and 20 mg/mL $\gamma$-$Fe_2O_3$, respectively), which can be scaled according to need.

**Table 1.** Optimum phospholipid content (0.88 SE; see text) for SML formation from 5 mL of 8.6 and 12.4 nm MNPs (10 and 20 mg/mL $\gamma$-$Fe_2O_3$, respectively, equivalent to 2.68 x $10^{16}$ MNPs in each case). The molecular area of DOPG is assumed to be 71 Å$^2$[42].

| Primary MNP size (nm) | Phospholipid for inner layer (µmoles) | Phospholipid for outer layer (µmoles) |
|---|---|---|
| 8.6 | 11.2 | 56.2 |
| 12.4 | 27.9 | 140 |

In step one, 5 mL of MNPs in benzyl alcohol were heated to 80 °C under $N_2$ with continuous magnetic stirring. 11% of the total phospholipid required to form the monolayer was added to the mixture in 1.5 mL MeOH, followed immediately by 1.5 mL of 35% $NH_4OH$. The remaining phospholipid (in 2 mL MeOH) was then added slowly over the course of 5 minutes. The mixture was stirred at 80 °C for a further 15 minutes before cooling to room temperature, magnetically decanting, and washing four times with 40 mL of a 50/50 MeOH/acetone solution. The wet sample was transferred to a clean reaction vessel and 10 – 12 mL of $H_2O$ was added. The volume of $H_2O$ used was varied to control the final Fe concentration of SML suspensions. At this stage, the suspension is not physically stable because addition of the outer phospholipid monolayer is not yet completed. In step two, the aqueous mono-SML sample was heated to 65 °C under $N_2$ with continuous magnetic stirring, and after 30 minutes at 65 °C, 30% of the phospholipid required to complete the bilayer was added in 1.5 mL MeOH, followed immediately by 1.5 mL 35% $NH_3$. In some cases, 0.1 mol% of the dialkyl fluorescent dyes DiD-DS or DiR-DS was included in the phospholipid mixture to permit labelling for *in vivo* monitoring of SML biodistribution in tissues. The remaining phospholipid, in 3.5 mL MeOH, was added slowly over the course of 5 minutes. The mixture was stirred at 65 °C for a further 25 minutes before being cooled to room temperature, sonicated for 30 minutes (Elma Ultrasonic), and magnetically separated over a standard neodymium (N52-type) magnet for 90 minutes to remove larger aggregates. A key formulation of interest are sterically-stabilised SML-PEG suspensions composed of 12.4 nm MNPs having a DOPG inner monolayer and an 85/15 mol/mol DOPC/DSPE-PEG-2000 outer monolayer, as this composition mimics that of FDA-approved liposomal products.

### 2.4 Removal of Non-Loaded Liposomes

Density gradient centrifugation (DGC) was employed to remove liposomes lacking MNP cores from SML suspensions. A step gradient was prepared by sequentially layering 0.5 mL of 10% dextran, 0.5 mL of 5% dextran, and then 0.5 mL of an SML suspension into a centrifuge tube. Samples were centrifuged for 90 minutes at 6000 g rpm, over which time the SML pelleted, whereas non-loaded liposomes lacked sufficient mass to penetrate the dextran bands. The supernatant was then removed and retained for quantification of residual ‘empty’ liposomes by HPLC (*Supplemental Information*). Typically, the pelleted SMLs were resuspended in 0.5 mL $H_2O$, but the volume can be varied to adjust SML suspensions to the desired Fe concentration. Experimentally, the centrifugation process can be repeated to confirm that the first DGC eliminated all non-loaded liposomes. Following DGC we find, by HPLC, that 72% of the total lipid used remains in the formulation, giving a final ratio of *c.*1 mg Fe/5 mg lipid.

## 2.5 Fast Field Cycling Nuclear Magnetic Resonance and $T_2$ Measurements

The $^1$H relaxation enhancements due to suspended magnetic nanoparticles were quantified based on the spin-lattice and spin-spin relaxivities, $r_1$ and $r_2$:

$$r_{1/2} = \frac{R_{1/2\,(meas)} - R_{1/2\,(solvent)}}{[Fe]} \qquad \text{Equation (1)}$$

where $r_{1/2}$ have units $s^{-1}$ $mM^{-1}$, $R_{1/2(meas)}$ and $R_{1/2(solvent)}$ are the measured relaxation rates of the suspensions and of the particle-free solvent, respectively, and [Fe] is iron concentration in mM. The $^1$H Larmor frequency ($\nu_L$) dependence of $r_1$ (the FFC-NMR profile) for the aqueous nanoparticle suspensions was recorded over the frequency range 0.01–40 MHz using a Stelar Spinmaster Fast Field Cycling NMR Relaxometer (Stelar SRL, Mede, Italy). The system operated at a measurement frequency of 16.3 MHz for $^1$H, with a 90° pulse of 7 μs. $T_1$ measurements were performed as a function of external field, $B_0$, with standard pulse sequences incorporating $B_0$ field excursions[43]. The temperature was set to 25.0±0.1 °C and allowed to equilibrate thermally for 10 minutes prior to measurement. For $13 < \nu_L < 40$ MHz a non-polarised experiment (NP/S) was employed, while in the lower frequency range ($0.01 < \nu_L < 13$ MHz), a pre-polarised experiment (PP/S) was employed[44].

## 2.6 MRI Analysis of MNP Formulations In Vitro

MR imaging was undertaken on a 4.7 Tesla preclinical MR imager utilising the ParaVision 3.0.2 imaging platform with a 35 mm I.D. radiofrequency transceiver coil (Bruker Biospin, Billerica, MA). Air temperature within the bore was maintained at 37 °C and samples were allowed to equilibrate thermally for 15 minutes prior to measurements. $T_2$ relaxation times (to evaluate $r_{2(\text{in vitro})}$) were measured using a CPMG spin-echo sequence with a fixed TR of 3000 ms, and measurements were carried out with varying TE, ranging from 20 – 1200 ms in 20 ms increments. Using Analyze 7.0 software (Analyze Direct, Overland Park, KS), regions of interest (ROIs) were drawn for recorded datasets and signal intensities were extracted using routines developed in house with MATLAB (Mathworks, Natick, MA)[45]. $R_2$ values were determined by fitting the extracted signal intensity as a function of TE using a single-exponential decay.

## 2.7 Preparation of Size-Defined Fluorescently Labelled Liposomes

As described previously, liposomes that mimic the composition of Doxil® and Onivyde® were prepared by a thin film hydration method using DSPC, DSPE-PEG-methoxy, and cholesterol in a 9:1:5 molar ratio, optionally including 0.01 mol% of the fluorescent, nonexchangeable dialkyl carbocyanine membrane labels DiD-DS or DiR-DS[18, 46]. The required lipids were dissolved in $CHCl_3$, and the $CHCl_3$ was removed slowly on a rotary evaporator to form a thin lipid film. The film was resuspended in preheated (45 °C) 140 mM NaCl/25 mM HEPES buffer (pH 7) at a phospholipid concentration of 20 mM with continued warming and vigorous vortexing. The resulting solution was sonicated for four 30-second intervals with intermittent warming and vortexing, subjected to 5 freeze-thaw cycles, and then extruded sequentially at 65 $^{o}$C through polycarbonate filters of decreasing pore size to produce liposomes of the required size range. Liposome diameter was measured by dynamic light scattering (NanoBrook Omni Analyser, Brookhaven Instruments, Holtsville, NY).

### 2.8 PDAC Tumour Models

Tumours derived from the PDAC cell line MIAPaCa-2, and patient derived xenograft (PDX) PDAC tumour models #18269, #18254 and #12424 were used as *in vivo* models[18, 19]. The PDX models were established at Roswell Park Comprehensive Cancer Center[47]. Small tumour fragments (*c.*8 $mm^3$) from donor mice were implanted subcutaneously on the abdominal wall of anesthetised 18-20 g CB17 SCID mice. Once tumours reached a volume of *c.*200 $mm^3$, mice were randomised into groups and studies were initiated. All procedures were approved in advance by the Institutional Animal Care and Use Committees of Roswell Park and the University at Buffalo, State University of New York.

### 2.9 IVIS Imaging

Prior to administration, SML suspensions were dialysed against 10% dextrose, subjected to 1 round of DGC, and the pellet was resuspended in 10% dextrose. DiD-DS-labelled SML-PEG formulations, prepared from 12.4 nm MNPs (TEM size) and having a DOPG // DOPC/DSPE-PEG (inner // outer monolayer) bilayer composition and $d_{hyd}$ of *c.* 100 nm were injected *iv* by tail vein into groups of n = 3 mice in volumes of ≤0.1 mL at a dose of 0.73 mg Fe per kg mouse body weight. Near-infrared fluorescence imaging was carried out on an IVIS® Spectrum *in vivo* imaging system (Perkin-Elmer) to determine biodistribution of DiD-DS labelled SML-PEG at varying timepoints. Regions of interest (ROIs) were drawn on the recorded images using Living Image Software (Perkin-Elmer) and fluorescence was quantified at 640/680 nm (ex/em).

## 2.10 In Vivo MRI Analysis of MNP Formulations

Mice were anesthetised with isoflurane, and body temperature and respiration rates were monitored continuously while imaging. $T_2$ measurements were carried out using a CPMG spin-echo sequence with a fixed TR of 5200 ms and TE values ranging from 10 –200 ms in 20 ms increments. Following geometry scans, the field of view (FOV = 32 x 32 mm) was aligned to ensure MR images were captured for the complete tumour volume, and slices 1 mm in thickness were recorded. The total acquisition time for each $T_2$ measurement was 23 minutes. Following acquisition of baseline scans, mice were injected with MNP formulations. Except where noted, groups for MRI experiments were n = 3 mice. MNP formulations (SML-PEG or FMX) in 10% dextrose were injected *iv via* the tail vein with an Fe dose of 50 mg/kg in volumes of ≤0.1 mL. $T_2$ weighted scans were then carried out at various timepoints. ROIs and $R_2$ values were determined from the MR images as described above. The reported $R_2$ values describe the average $R_2$ value across the whole tumour volume, whereas $\Delta R_2$ values describe the change in $R_2$ of the tumour at a given timepoint with respect to the baseline scan (pre-injection).

In some experiments, mice were pre-treated with a *SMO* inhibitor (sHHi) to increase tumour permeability/perfusion and SML deposition in the PDX models[17-19]. The sHHi NVP-LDE225 was dispersed at a final concentration of 4 mg/mL in 0.5% (w/v) methyl cellulose and 0.5% Tween-80 in sterile $H_2O$ using sonication. N=3 mice per sHHi treatment group were dosed *po* daily by gavage with 40 mg/kg/day sHHi for 5 days prior to SML treatment.

## 2.11 Quantification of SML Deposition in PDAC Models by Fluorescence Microscopy

Tumours embedded in OCT (optimal cutting temperature compound) were sectioned using a Leica CM1850 Cryostat at -20°C. Sequential 10 μm sections were taken at three different depths within the tumour, *c.* 200 – 300 μm apart. Tumour sections were allowed to dry at room temperature for 10 minutes, co-stained with DAPI, and mounted. Images were acquired on a

Leica DM-6B fluorescence microscope, and intratumour distribution of SML-PEG was quantified using FIJI (ImageJ) software[48, 49]. To exclude large mucinous vacuoles that appear as voids in images of some PDAC PDX tumours, tumour cell-containing areas were segmented for quantification by generating a mask of the cell-containing regions based upon DAPI staining of nuclei, and the fluorescence intensity and fraction of the area occupied by SML-PEG (A%) was quantified within the cell-containing regions within multiple tumour sections (n=3) from each replicate animal. The A% reflects the distribution of SML-PEG within the tumour section, whereas the fluorescence intensity represents the magnitude of tumour deposition.

### 2.12 Quantification of Iron Content

Total iron content of the SML suspensions was determined by atomic absorption spectroscopy, using a Varian SpectrAA 55B atomic absorption spectrometer fitted with a single slit burner. The light source was an Fe-cathode lamp with a wavelength of 248.3 nm, and a high-temperature air/acetylene flame was used. MNP samples were prepared for analysis by acid digestion. Typically, a 20 – 100 µL aliquot of sample, depending upon estimated concentration, was placed in a volumetric flask, to which 1.5 mL of 12 M concentrated HCl was added. The samples were allowed to digest for 2 hours, and then diluted to a final volume of 50 mL with 1 M $HNO_3$.

ICP-MS was used to determine Fe concentrations in PDAC tumour tissue following SML treatments, employing a modification of [50]. To ensure sample homogeneity, tumours were ground under liquid nitrogen and *c.* 100 mg of the powder was weighed and placed in 15 mL centrifuge tubes. 1 mL of 12 M HCl and 3 mL of 16 M $HNO_3$ were added, and the samples were allowed to digest for 1 hour at room temperature. Then the samples were heated in an oven at 60 °C for 2 hours and allowed to cool. Samples were diluted to appropriate concentrations with 1 M $HNO_3$, and submitted to the National Centre for Isotope Geochemistry, University College Dublin, for ICP analysis. Measurements were carried out on an iCAP-Q ICP-MS (ThermoFisher) in high matrix and collision cell mode, using He as the collision cell gas (4.85 mL/min). Samples were introduced into the mass spectrometer through a cyclonic, Peltier-cooled spray chamber with an ESI PFA-ST nebuliser at a rate of 100 µL/min, and $^{56}$Fe and $^{57}$Fe were quantified. Washes between samples consisted of 80 seconds of 5% $HNO_3$ with an accelerated peristaltic pump, followed by 80 seconds of sample uptake. External standards were diluted from a Sigma-Aldrich TraceCert periodic table mix 1 (Lot #BCBR7889V) over a concentration range of 1 - 400 ppb, with sample standardisation carried out every 20 to 30 samples to account for instrumental drift. Data was processed using the QTegra software package (ThermoFisher).

### 2.13 SML Characterisation

A Malvern Instruments NanoZS (Malvern UK) was used for dynamic light scattering (DLS) measurements at a temperature of 25 °C. The light source was a 3 mW He–Ne laser operating at a wavelength of 633 nm, and back-scattered light was detected at an angle of 173° to the incident beam. The z-average and polydispersity index (PDI) values were calculated using cumulants analysis[51]. The cumulants model fitted the correlograms well in all cases, and there was no indication of larger aggregates in the Mie analysis. Therefore, the z-average was used as a measure of the mean hydrodynamic diameter ($d_{hyd}$). It was not possible to record $d_{hyd}$ for dye-loaded SMLs or liposomes because of their high absorption. Therefore, DLS measurements were carried out on dye-free SMLs that were prepared in parallel.

Fourier transform infrared (FT-IR) analysis was undertaken on dry powder samples using a Vertex 70 FT-IR spectrometer equipped with a Globar Infrared source for a NIR-MIR spectral range, a DRIFTS (Praying Mantis) cell, and a liquid nitrogen-cooled mercury cadmium telluride detector. Features in recorded spectra were assigned to their corresponding chemical structures based upon[52].

## 2.14 Statistical Analysis of Datasets

MRI and fluorescent microscopy results were tested statistically using a two-tailed unpaired t-test at a 95 % confidence interval. In figures and tables, * indicates $P<0.0332$, ** indicates $P<0.0021$, *** indicates $P<0.0002$ and **** indicates $P<0.0001$.

# 3. RESULTS AND DISCUSSION

## 3.1 Preparation and Characterisation of SML Suspensions

The optimised preparation method provides stable, aqueous suspensions of bilayer-coated SMLs. One key advantage of this approach is separating MNP synthesis from the SML formation step (Figure 1a), which allows production of size-controlled primary MNPs having improved crystallinity (and hence magnetisation), as compared to co-precipitation alternatives. The surfactant-free thermal decomposition approach[26] used here provides MNPs ($d_{TEM}$ 8.6±2.0 nm) within the superparamagnetic size range[53], having weakly-associated solvent (benzyl alcohol) molecules that can be easily replaced by a stabiliser of choice. The two-step approach represents a significant advance on our previous work[25], because the magnetic- and magnetic resonance properties are improved, and can be tuned for a given cluster size by selection of the appropriately-sized primary MNP.

In the first step of SML formation, the MNP clusters were coated with chemisorbed DOPG to form intermediate ‘mono-SML’ suspensions stabilised with alkyl chains that are probably fully extended in $CHCl_3$ under the largely solvophilic conditions (*Experimental* and Figure 1a). Addition of a monolayer surface-equivalent (SE 1.00) of DOPG produced partially aggregated MNPs, and stable SML suspensions having sub-100 nm hydrodynamic size, $d_{hyd}$, were formed only when an optimal surface equivalent of DOPG, SE 0.88, was used for the inner monolayer (see *Methods*). Our interpretation is that this SE provides a full chemisorbed lipid monolayer (close to complete coverage) for each MNP in the final SMLs. DLS size distributions for mono-SMLs are shown in Figure 1b; the average $d_{hyd}$ was 80 nm, but the suspensions were polydisperse (PDI 0.54), with a main feature at 44 nm and a small sub-population of large aggregates. The formation of mono-SMLs and the absence of free DOPG was demonstrated by FTIR (Figure S2a and Table S2), which showed a lack of spectral features arising from the free phospholipid head group (absence of bands for $PO^2$).

In the second step of SML formation, a stable membrane bilayer was completed by physisorption of an outer monolayer of the desired composition with phase transfer into water, thereby producing the final, stable 'SML' aqueous suspensions (*Methods)*. In Figure 1, the phase transfer was completed using DOPC to provide suspensions designated 'DOPG // DOPC SML' (inner // outer layer composition). These aqueous suspensions are far more monodisperse than those of mono-SML and have larger average $d_{hyd}$ (*c.*73 nm) and lower PDI (0.23). We attribute the improved monodispersity and colloidal stability to the presence of a complete physisorbed outer monolayer. The apparent increase in average hydrodynamic size from *c.*44 nm (mono-SML in $CHCl_3$) to *c.*73 nm (DOPG // DOPC SML in $H_2O$) is consistent with addition of a second phospholipid monolayer, with little change in the number of particles per cluster. The presence of a phospholipid bilayer on SMLs was also evidenced with FT-IR by the observed bands of exposed phospholipid head groups ($PO^{2-}$) in the DOPG // DOPC SML spectrum (Figure S2b and Table S3).

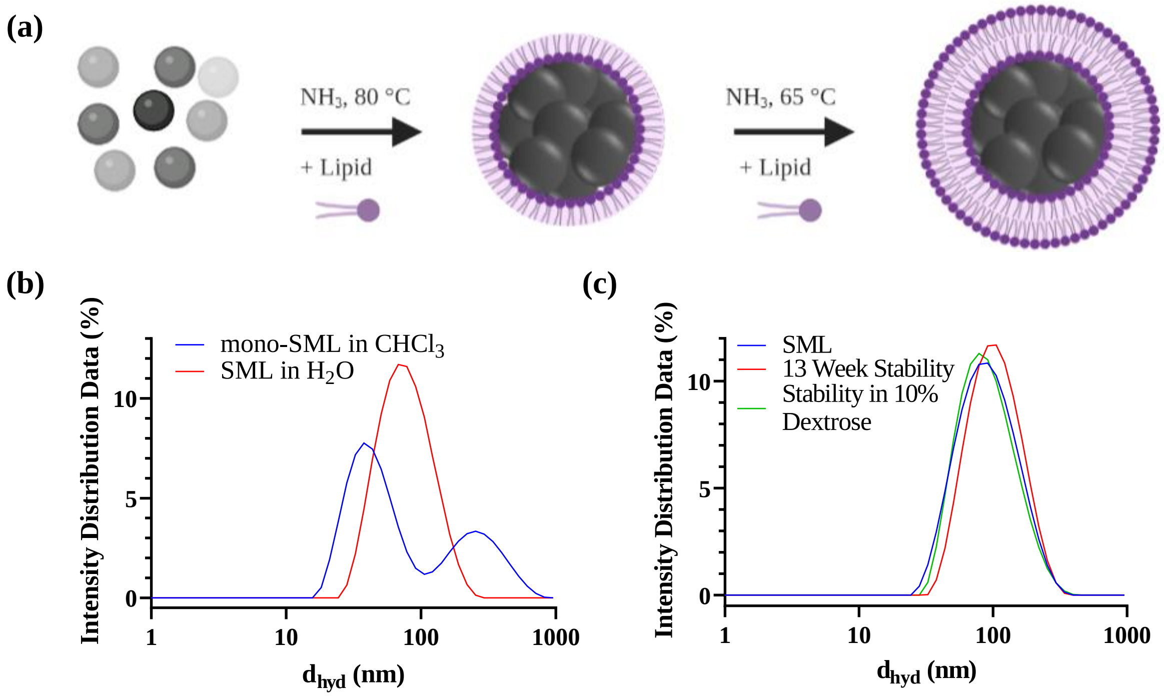

**Figure 1. (a)** Schematic representation of SML preparation. **(b)** Representative size distribution by DLS of mono-SML suspensions ($CHCl_3$, $d_{hyd}$ 80 nm, PDI 0.54) and bilayer-coated SMLs composed of 8.6 nm primary MNPs with a DOPG // DOPC (inner // outer) phospholipid bilayer ($H_2O$, $d_{hyd}$ 73 nm, PDI 0.23). An SE of 0.88 was used for mono-layer formation. **(c)** Stability of the size distribution of an SML suspension composed of 8.6 nm MNPs having a DOPG//DOPC phospholipid bilayer, showing retention of its monodispersity in water over 13 weeks at room temperature and in 10% dextrose.

DLS confirmed that DOPG // DOPC SML suspensions are stable from batch-to-batch, with size distributions unchanged over 13 weeks, and only a slight increase in $d_{hyd}$, in isotonic 10% dextrose, which is suitable for parenteral administration (Figure 1c). We have previously shown by cryo-SEM that DOPC // DOPG stabilised MNP clusters have spherical morphology, consistent with densely-packed MNP clusters[25]. DOPG was identified as the lipid of choice for the inner monolayer as it afforded suspensions with the best long-term colloidal and chemical stability, likely due to the high affinity of the anionic phospholipid headgroup for the iron oxide surface. The outer monolayer composition was highly flexible; Table S4 demonstrates the general applicability of the approach to produce a library of SML suspensions from different-sized primary MNPs and different outer leaflet compositions that are colloidally stable. This compositional flexibility was exploited (*below*) for inclusion of both stable membrane dye labels and anchoring a sterically-stabilizing polymer coat (SML-PEG). Numerous other functionalities could be designed into these SML, such as inclusion of di-alkyl/acyl anchors for covalent surface attachment of reporter molecules or affinity targeting ligands[54].

A key formulation of interest are sterically-stabilised SML-PEG suspensions composed of 12.4 nm MNPs (TEM size) having a DOPG inner monolayer and an 85/15 mol/mol DOPC/DSPE-PEG-2000 outer monolayer, as this composition mimics that of FDA-approved liposomal products[13]. FT-IR analysis confirmed the incorporation of DSPE-PEG-$NH_2$ in the phospholipid bilayer of DOPG // DOPC/DSPE-PEG-$NH_2$ SMLs by the presence of a feature in the FT-IR spectrum assigned to $NH_2$ stretching modes at 3674 $cm^{-1}$ (Figure S2b, Table S3). The reduction in the intensities of several spectral features (including C=O stretch at 1740 $cm^{-1}$ and CH scissoring at 1450 $cm^{-1}$, both arising from the lipidic chain) are attributed to the presence of the DSPE-PEG-2000 (15 mol% in the formulation) which has previously been shown to dampen these features[55].

The MNP / phospholipid ratio used in both steps of formation was critical. As noted above, an optimal lipid-equivalent (SE 0.88) is needed for the inner monolayer to ensure colloidal stability. It is likely that any lipid deficiency compromises colloidal stability in $CHCl_3$, whereas lipid excess results in a partial (physisorbed) outer layer that disrupts subsequent bilayer formation. However, formation of stable SML suspensions was challenging without a significant excess of external leaflet lipid. During bilayer formation, excess phospholipid could theoretically promote the formation of un-loaded liposomes within the SML formulation, which could compete *in vivo* with biodistribution of SMLs. Therefore, we developed a density-gradient centrifugation (DGC) method to quantify possible un-loaded liposomes, and to remove any lower-density unloaded liposomes from higher-density SML preparations. Post-DGC, the low-density phospholipid fraction was *c*.28% of the total lipid (Experimental), and one round of DGC removed the vast majority of iron-free phospholipid without removal of any iron from the SML suspensions (Figure S3). Only a small increase in $d_{hyd}$ was observed following DGC (from 99 to 105 nm), and both monodispersity and long-term colloidal stability were retained (Figure S4). Repeated DGC also confirmed that unloaded liposomes do not reform over 8 weeks.

There are several reports of preparation of magnetoliposomes by thin film rehydration in the presence of an excess of MNPs. Most of these describe densely packed MNPs within an aqueous lumen,[21] or more rarely very small MNPs within the bilayer,[56] as opposed to a 'solid core'. To the best of our knowledge, apart from our earlier study,[25] there are no reports of (lumen free) solid cores of MNPs with lipid bilayers. If lumens form they have been shown to unstable osmotically, with resulting size changes determined by the local environment,[57] that are difficult to predict. It is interesting that there are reports of removal of uncoated MNPs is some of these cases,[58-61] but not of free lipid. For SML suspension there are no uncoated MNPs present (they would not be colloidally stable under these conditions), but there is the opposite necessity of removing unloaded liposomes by DGC, as a lipid excess was required to generate the colloidal stability needed.

### 3.2 MR Relaxivity of SML Suspensions

The magnetic resonance properties of SML suspensions were evaluated to determine their capabilities as MRI contrast agents. The $^1$H spin-lattice relaxivity, $r_1$, which is defined as the water relaxation rate enhancement per mM Fe concentration, was measured as a function of the $^1$H Larmor frequency ($\nu_L$) using fast-field cycling NMR relaxometry (FFC-NMR). The high frequency $r_1$ is a measure of the potential to generate contrast under the appropriate weighting conditions in MRI, and the dependence of $r_1$ on $\nu_L$, the FFC-NMR profile, provides insights into the internal magnetic ordering/dynamics of magnetic clusters[62, 63]. Figure 2a shows the recorded profiles of an SML-PEG suspension composed of 12.4 nm primary MNPs, with a diameter of 92 nm (PDI 0.23) and a DOPG // DOPC bilayer. For comparison, a profile reported previously[25] is shown for SMLs composed of 13.8 nm MNPs, prepared by coprecipitation methods, having a DOPG // DOPG bilayer (90 nm, 0.20), along with a simulated profile for fully dispersed 12.4 nm MNPs, generated using a model developed by Roch, Muller and Gillis[64]. Simulation was required because the lipid-stabilised primary

MNPs do not disperse fully in $H_2O$. The approach employed is generally accepted, and for particles in this size range, we have demonstrated that it provides good consistency with independently recorded magnetometry and electron microscopy data[65].

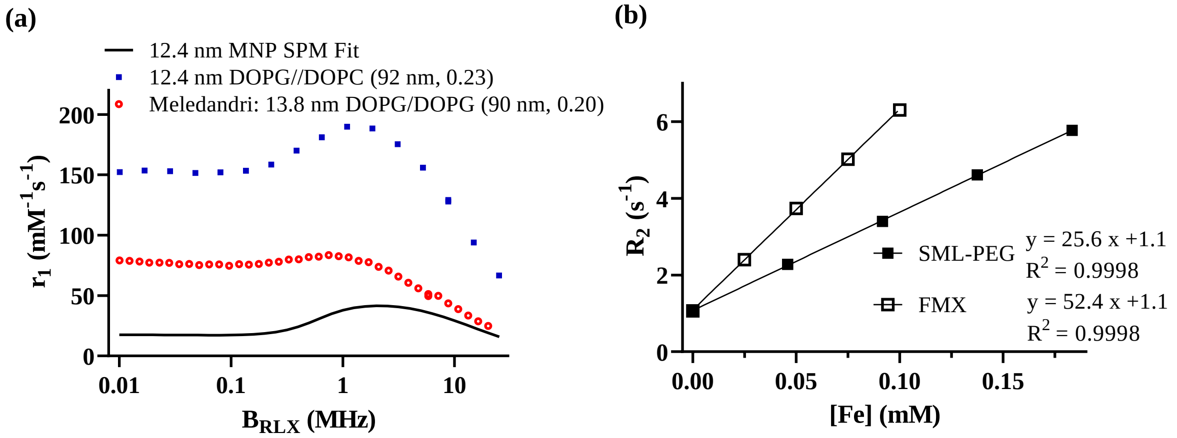

**Figure 2. (a)** Blue squares: FFC-NMR profiles of frequency vs. $r_1$ at 25 °C for an SML suspension composed of clustered 12.4 nm primary MNPs within a DOPG // DOPC bilayer (diameter 92 nm, PDI 0.23). Red circles: profile of an SML suspension composed of 13.8 nm primary MNPs prepared by coprecipitation methods with a DOPG // DOPG bilayer (diameter: 96 nm, PDI 0.16), adapted from [24]. Solid line: simulated profile for 12.4 nm MNPs with $d_{NMR}$ 8.0 nm, $\tau_n$ 12 ns, $M_s$ 37 emu $g^{-1}$ and $\Delta E_{anis}$ 1.5 GHz (details in Figure S5). The simulation is necessary because a fully dispersed particle suspension cannot be generated without changing the surface chemistry. **(b)** $R_2$ values for FMX and SML-PEG (12.4 nm primary with a DOPG inner monolayer and an 85/15 mol/mol DOPC/DSPE-PEG-2000 outer monolayer) as a function of Fe concentration at 37 °C and 4.7 T (200 MHz), recorded on the MRI scanner.

The difference between the profile recorded for 92 nm SMLs (Figure 2a, blue) and the simulation for fully dispersed particles (black line) confirms the absence of any single particles in the suspension, consistent with DLS analysis. The significant increase in relaxivity at all frequencies, and in particular at high frequency, demonstrates the potential of SMLs to provide MRI contrast. The effect arises due to an increased cluster moment, compared to that of dispersed particles. Clustering also changes the moment dynamics; the shift in the $r_1$ maximum to lower frequencies (from 2.0 MHz to 1.5 MHz) results from greater diffusional (Brownian) contact time ($\tau_B$) of $H_2O$ with the nanostructure. The large increase in $r_1$ at lower frequencies arises from increased Néel correlation time, $\tau_N$, the timescale for re-orientation of the moments attributed here to dipolar interactions within the clusters. Similar effects have been reported for suspensions of fatty acid-stabilised MNP clusters[62]. A profile for similarly-sized SMLs, prepared using co-precipitation methods we reported previously[25], demonstrates the advantages of the two-step SML preparation (Figure 2a, red). Increased particle magnetisation (and hence crystallinity) is confirmed by the significantly improved $r_1$ at all frequencies for clusters that are very similarly sized. Finally, inclusion of 15% DSPE-PEG-2000 into the outer phospholipid monolayer had little effect on the profile shape (Figure S5). Thus, SMLs have considerable flexibility in terms of outer monolayer composition without significantly altering their colloidal stability or relaxivity.

SML-PEG suspensions were evaluated for their potential as MRI contrast agents under $T_2$-weighted conditions by measuring their $^1$H spin-spin relaxivity *in vitro*, $r_{2(\text{in vitro})}$, using an MRI scanner at 4.7 T (200 MHz) and 37 °C. FMX was included as a commonly-studied comparator, as it has been used as a contrast-agent in numerous preclinical $T_2$-weighted MRI studies[36, 37]. It consists of superparamagnetic iron oxide MNPs stabilised with a carboxy-dextran coating, having a $d_{hyd}$ value of *c.* 30 nm (PDI 0.20). Figure 2b shows $R_2$ values of SML-PEG and FMX as a function of Fe concentration. The responses are linear, and regression provides $r_{2(\text{in vitro})}$ values of 52.4 and 25.6 $mM^{-1}s^{-1}$ for FMX and SML-PEG, respectively. $R_{2(H2O)}$ values of 1.1 $s^{-1}$ were determined in both cases, which is in the expected range for pure water. SML-

PEG have approximately half the $r_{2(\text{in vitro})}$ of FMX, which should be sufficient for generating contrast *in vivo,* particularly in cases in which the PEG surface coating provides elevated tumour deposition; detectable differences in MRI contrast depend not only on the inherent relaxivity, but also on local deposition and the effect of the microenvironment on the particles following deposition (*below*).

### 3.3 SML Biodistribution

The in vivo experiments described below focus upon sterically-stabilised SML-PEG suspensions composed of 12.4 nm MNPs (TEM size) having a DOPG inner monolayer and an 85/15 mol/mol DOPC/DSPE-PEG-2000 outer monolayer, unless otherwise stated. To assess SML-PEG deposition in PDAC tumours, mice were implanted with MIAPaCa-2 cells, and when tumours reached an initial threshold volume of 150-300 $mm^3$, SML-PEG (DOPG // DOPC/DSPE-PEG, as above), resembling Doxil® or Onivyde® liposomes in terms of outer membrane leaflet composition, were labelled with the non-exchangeable fluorescent membrane label DiD-DS and injected *iv* in n=3 mice/group. Non-invasive fluorescence (IVIS) imaging was employed at intervals to quantify their deposition in tumours and tissues of the RES (liver, lung, spleen; Figure 3a). The temporal and biodistributional characteristics of SML-PEG were similar to those described for Doxil® liposomes[66]. Fluorescence appeared rapidly in both tumour and liver, but liver uptake saturated within 4h post-dose, whereas SML-PEG continued to accumulate in the tumour over 24 hours (Figure 3b). Thus, after rapid initial accumulation of a fraction of SML-PEG in RES tissues, a significant quantity remained in circulation and underwent additional tumour deposition and showed the delayed peak accumulation in tumours characteristic of Doxil®-type liposomes.

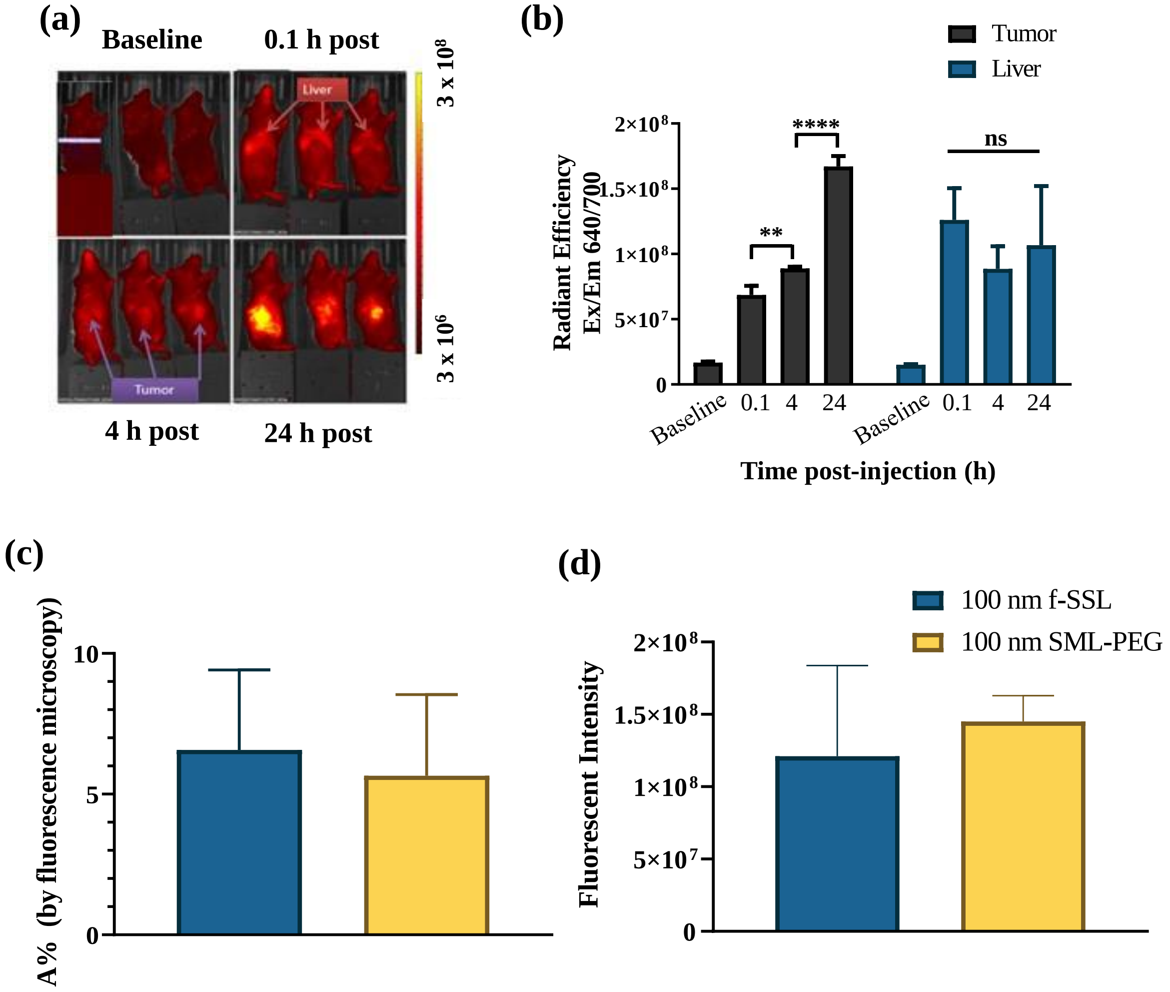

**Figure 3. (a)** IVIS images of 100 nm SML-PEG biodistribution in SCID mice bearing MIAPaCa-2 PDAC tumours (n = 3 mice at an Fe dose of 0.73 mg/kg). Tumour deposition increased over time, whereas liver deposition peaked shortly after injection. **(b)** Corresponding quantification of SML-PEG in tumour and liver from IVIS images at 0, 4, and 24 hours post injection, showing continuously-increasing deposition in the tumour. Increases over baseline were significant for both tumour and liver, as were the temporal increases in tumour deposition (*, $P < 0.0332$; **, $P<0.0021$; ****, $P<0.0001$; ns, not significant). (**c-d**) Mice bearing PDAC PDX #18269 (n=3/group) were injected *iv* with 100 nm SML-PEG or fluorescent SSL (1 µg lipid/animal) of equivalent diameter and outer membrane leaflet/bilayer composition. After MR imaging (below), tumours were harvested at 24 hours post-injection, flash-frozen, sectioned, and fluorescence marker deposition was quantified by microscopy. **(c)** Fraction of the tumour penetrated by SML-PEG or f-SSL (area occupied by fluorescence normalised

by the total area occupied by tumour in each tissue section), and **(d)** their overall magnitude of deposition, based upon fluorescence intensity. Mean area of tumour deposition and magnitude of deposition were statistically indistinguishable for the two formulations.

Cell line-based tumours are well-accepted models for investigation of nanoparticle pharmacokinetics and biodistribution, but typically have higher vascular density and permeability and lack the stromal desmoplasia of PDAC. To test the hypothesis that SML-PEG constructed with an outer bilayer leaflet resembling the composition of Doxil® or Onivyde® liposomes would undergo similar tumour deposition, we compared the tumour deposition of DiD-DS-labelled SML-PEG (DOPG // DOPC/DSPE-PEG bilayer; Figure 3a-b) with that of fluorescent SSL (f-SSL; DOPC/DSPE-PEG) in mice (n=3/group) bearing PDAC PDX #18269, which has stromal desmoplasia and microvessel density comparable to clinical PDAC samples[19]. Tumour deposition was quantified by fluorescence microscopy of multiple tissue sections in replicate animals 24 hours post-injection. Representative fluorescence images are provided in Figure S6. The A% (area of tumour in which fluorescent nanoparticles were detected, relative to total tumour area in the same field) occupied by SML-PEG or f-SSL was quantified, as was magnitude of deposition, based upon fluorescence intensity. Figure 3c-d shows very similar, statistically-equivalent tumour deposition 24 hours after administration, both in terms of magnitude of deposition and the physical extent to which the fluorescent particles distributed within the tumour. Although *in vitro* investigations of particle flow through microfluidic channel models of microcirculation[67] suggested that higher particle density reduces marginalisation toward microvessel walls, particle extravasation and deposition within these PDAC tumours did not differ significantly for SML-PEG and f-SSL. The results suggest that particle diameter and outer layer composition are the key determinants of biodistribution for these materials in these clinically-relevant models.

### 3.4 *In vivo* MR Imaging Performance

The potential of SML-PEG (12.4 nm MNPs; DOPG // DOPC/DSPE-PEG bilayer; $d_{hyd}$ *c.* 100 nm, PDI *c.* 0.2) for evaluating PDAC perfusion/permeability and predicting tumour deposition of nanoparticulate therapeutics was assessed *in vivo* with a series of PDAC PDX models that recapitulate the inter-patient characteristics and variability of the clinical disease. The models included PDX #18269 (high-stroma/moderate vascularity/slow growth rate), #18254 (high stroma/low vascularity/slow growth rate), and #12424 (moderate stroma/low vascularity/ moderate growth rate). SML-PEG were also evaluated for their potential to detect transient changes in tumours induced by stroma-modulating strategies that have been demonstrated to increase permeability/perfusion in PDAC models, such as SMO inhibitors of sonic hedgehog (sHH) signalling. The embryonic sHH signalling pathway is reactivated in most PDAC tumours, and functions as a paracrine network, in which tumour cells activate tumour-associated stromal cells, driving stromal amplification (desmoplasia) and increasing intratumour pressures that collapse vasculature, reducing perfusion, permeability, and drug delivery[17-19, 68]. SMO inhibitors of sHH signalling (sHHi) decrease extracellular matrix production and stromal density, restoring tumour perfusion/permeability, and enhance drug and nanoparticle delivery[17-19]. However, their clinical development has been hampered by inter-patient variability in response to the ‘tumour priming’ effects of sHHi[69, 70]. Non-invasive approaches to identify patients whose tumours are accessible to nanoparticulate drug carriers, or respond to stroma-targeted ‘priming’ approaches would advance clinical development and efficacy of PDAC therapies.

Mice bearing PDX #18269 tumours, which respond to sHHi pre-treatment with increased nanoparticle deposition and greater therapeutic efficacy of antibodies or drug-containing nanoparticles [18, 19] were imaged at baseline, injected *iv* with SML-PEG (50 mg/kg Fe dose) and then the change in tumour $R_2$ ($\Delta R_2$) was obtained from $T_2$-weighted images acquired 24 hours later (Figure 4a). Deposition of SML-PEG increased in sHHi pre-treated animals relative to controls; based upon $\Delta R_2$ values (Figure 4b), contrast enhancement nearly tripled (2.0±1.7 *vs*. 5.9±2.4 $s^{-1}$) with sHHi pre-treatment, confirming the potential of SML-PEG to report therapeutically-important effects of stromal modulation upon tumour nanoparticle deposition.

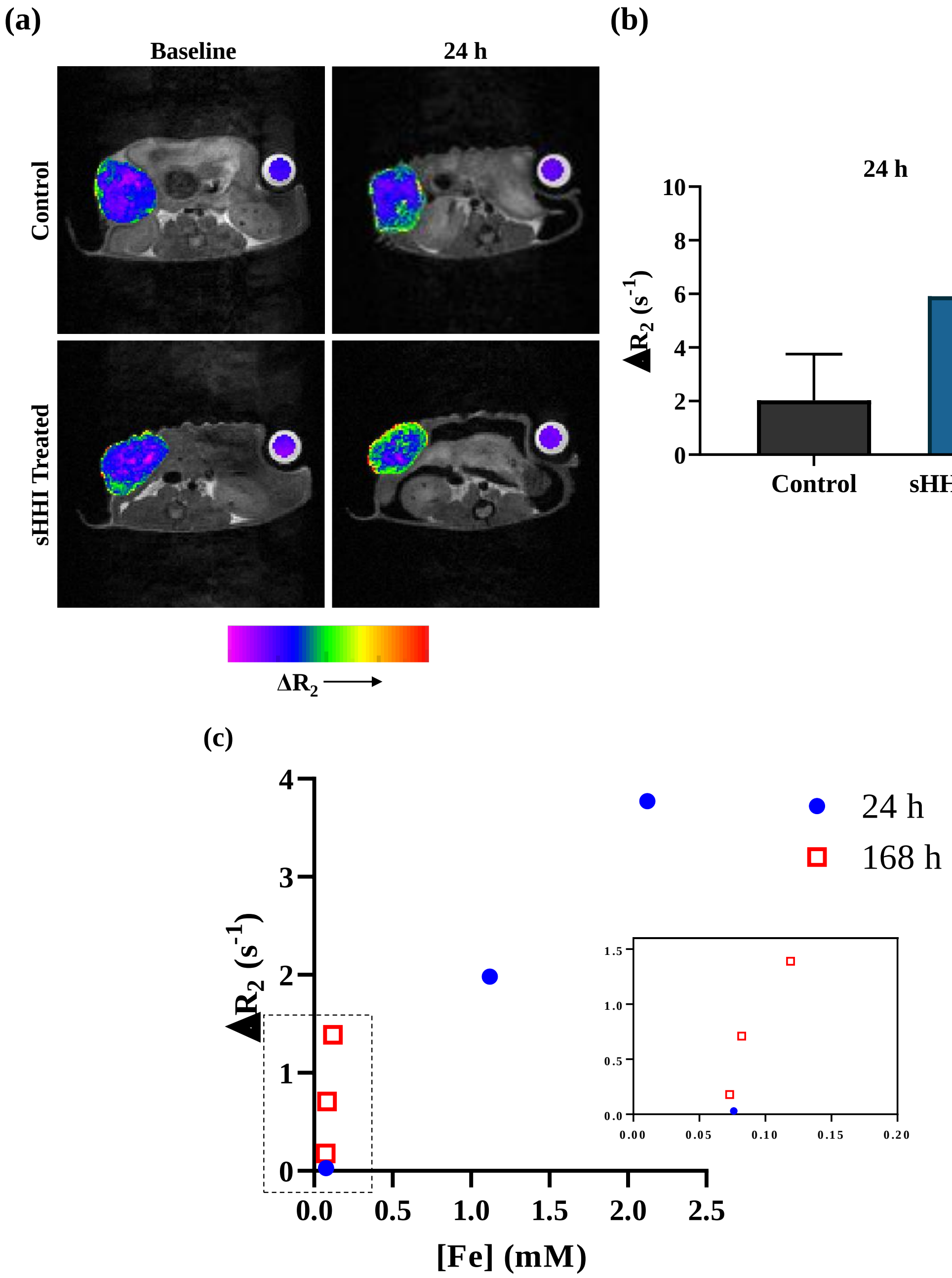

**Figure 4. PDAC tumour accumulation of SML-PEG.** Mice bearing PDAC PDX tumour #18269 were pre-treated daily with vehicle or 40 mg/kg sHHi NVP-LDE225 (n=3/group) for 5 days prior to imaging and *iv* SML-PEG injection. **(a)** Representative MRI slices of tumours overlaid with $R_2$ maps before and 24 hours after SML-PEG injection (Fe dose 50 mg/kg) in control and primed (sHHi) mice. **(b)** Average recorded $\Delta R_2$ for #18269 tumours (n = 3) 24 hours after SML-PEG injection in control and sHHi-primed mice, showing a *c.* 3-fold increase following sHHi-priming. **(c)** Comparison of tumour $\Delta R_2$ with Fe concentration for n=3 untreated control mice at 24 or 168 hours after SML-PEG injection.

The inset shows an expansion of the identified region of the main panel. The endogenous Fe content of blank tumours (*c.* 0.07±0.03 mM) was subtracted from each sample; reported values reflect tumour deposition of SML-PEG. Average Fe content was 1.11 ± 1.02 mM at 24 hours, and 0.09 ± 0.02 mM at 168 hours.

The long-term *in vivo* behaviour of SML-PEG was also investigated. At 24 and 168 hours after SML-PEG administration to control (untreated) mice, n=3 mice were imaged, and tumour Fe was quantified by ICP-MS. The endogenous Fe content of blank tumours was measured (*c.* 0.07±0.03 mM) and tumours treated with SML-PEG were corrected so the reported values below reflect tumour SML-PEG deposition. As expected, there was significant inter-individual variability in Fe deposition and MRI response in these un-primed tumours (Figure 4c). SML-dependent contrast enhancement persisted over 168 hours, with $\Delta R_2$ in the range from 1.1±0.6 $s^{-1}$ as compared to 1.9±1.8 $s^{-1}$ at 24 hours post-injection (Figure 4c); at 24 and 168 hours, the Fe concentration was *c.* 17- and 2-fold higher than background. For each animal at both time points, $\Delta R_2$ varied linearly with Fe content. Whereas tumour Fe content decreased *c.*12-fold over 24-168 hours, $\Delta R_2$ values only decreased *c.*2.5-fold. The relationship, if any, between *in vitro* relaxation values ($r_{2(\text{in vitro})}$) and the time-dependent relaxation enhancements *in vivo* in the tumour environment is not well described for any agent. Based upon the $\Delta R_2$ values and Fe content of the tumours, $r_{2(\text{in vivo})}$ values were estimated for SML-PEG at both time points. The resulting average effective relaxivities were 1.8±1.5 $mM^{-1}s^{-1}$ at 24 hours, and 8.9±4.6 $mM^{-1}s^{-1}$ at 168 hours post injection, suggesting that extended exposure to the tumour environment, most likely resulting in degradation of the lipidic bilayer, leads to a *c.*5-fold increase in $T_2$ efficacy of the SMLs. Magnetic particle imaging (MPI) offers a potential alternative non-invasive approach to quantifying particle deposition in situ that is insensitive to endogenous Fe, potentially enabling study of the effect of the tumour microenvironment on MNPs. In MPI a strong static field is applied and a field free spot is then rastered through the subject; magnetic relaxation of particles entering the spot enables their quantification [71]. Low particle number detection is possible but spatial resolution is currently lower than for MRI [72], nevertheless the potential is promising [73].

To evaluate intratumour deposition and distribution of SML-PEG spatially within tumours, the nanoparticle membranes were trace-labelled with a non-exchangeable fluorescent probe and administered to tumour-bearing mice that were pre-treated with sHHi or vehicle for 5 days. Tumours were harvested 24 and 72 hours after *iv* injection, bisected, flash-frozen in mounting medium, sectioned, and imaged (Figure 5a). At 24 hours post-injection, which is typically the peak tumour deposition time for SML, SML-PEG were observed in the extensive stromal regions of the tumour that are characteristic of PDAC. Over 72 hours, fluorescence declined. In sHHi pre-treated tumours, SML-PEG deposition appeared greater and more uniformly-distributed, and fluorescence remained high 72 hours after injection. The fraction of the tumour tissue area (A%) into which SML-PEG distribute after extravasation was quantified from multiple tumour sections of each replicate animal (Figure 5b). The data show that SML-PEGs accessed a higher proportion of the tumour volume in sHHi pre-treated animals, compared to untreated controls, indicating increased tumour deposition and intratumour distribution. Furthermore, sHHi treatment increased the intratumour residence time of SML-PEG, as indicated by their statistically greater retention 72 hours post-injection, consistent with previous data suggesting that sHHi pre-treatment enhances convective delivery of therapeutic antibodies to PDAC tumours, and that clearance by back-diffusion to the vasculature is comparatively less efficient[19]. Thus SML-PEG as a nanoparticulate imaging agent appears to reflect both intrinsic tumour susceptibility to nanoparticle delivery, as well as therapeutically-relevant modulations of tumour vascular permeability and perfusion by stroma-remodelling treatments.

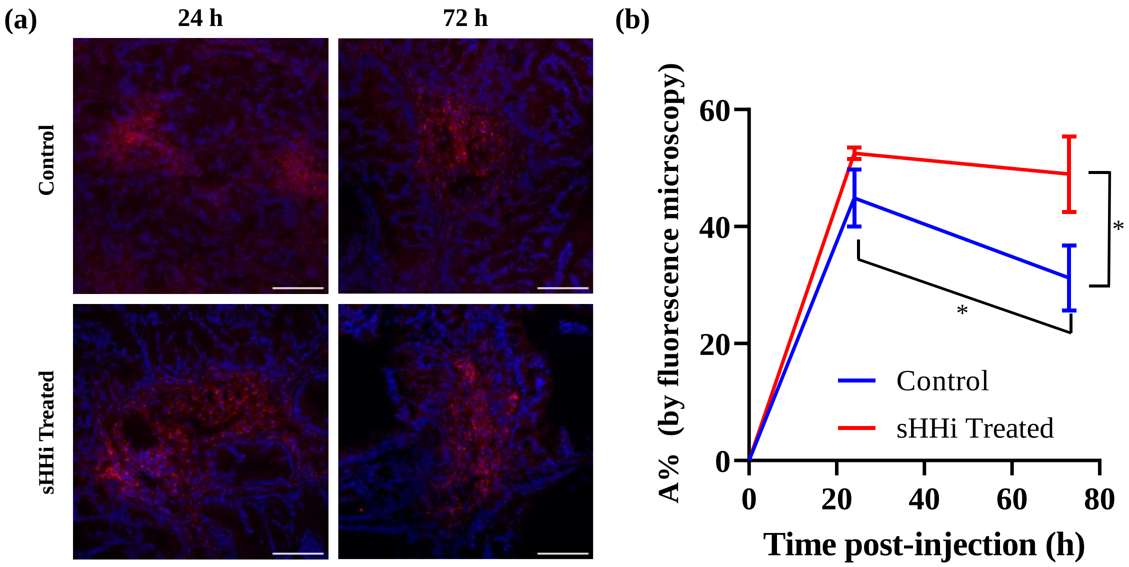

**Figure 5. (a)** Representative fluorescence microscopy images of #18269 tumours in control- and sHHi-pretreated mice (n=3/group) 24 and 72 hours after *iv* injection of DiD-DS labelled SML-PEG (red). Tumours were bisected, flash-frozen, sectioned, and imaged. DAPI was included in the mounting medium to counterstain nuclei (blue). The images were acquired under identical conditions to permit comparison of intensities and distribution. Scale bar: 100 µm. **(b)** The area the cell-containing (DAPI$^+$) tumour regions in which SML-PEG underwent deposition (A%) was quantified from multiple tumour sections in replicate animals. The prominent void s representing fluid-filled glandular structures that contain no cells (*eg.* lower left panel in 5a) were excluded from the area calculation. The data show greater persistence and % area coverage of SML-PEG in sHHi-pretreated animals (* indicates P<0.0332).

Deposition of DiD-labelled SML-PEG with similarly-sized f-SSL ($d_{hyd}$ *c.* 100 nm) containing DSPE-PEG-2000, which resemble closely the composition of clinically-approved SSL products such as Doxil® and Onivyde® was compared to test the applicability of SML-PEG as a predictor of vascular permeability. Representative PDAC PDX models (#18269, #18254 and #12424) were selected to capture inter-patient differences in their disease in terms of growth rate, quantity of stroma, and microvessel density (MVD). These models have been characterised, their driver mutations were previously reported and they have been shown to retain stromal amplification (desmoplasia) through multiple passages, and importantly retain the histological characteristics of the original patient tumours, particularly the very low permeability/perfusion and high tumour-to-blood vessel distances of clinical tumours [18, 19, 47, 74-76]. In relation to the models used within this work, PDX #18269 showed high MVD/high-stroma, #18254 had low MVD/high-stroma, and #12424 displayed high MVD/low-stroma.

The greatest tumour deposition levels, as indicated by the recorded fluorescent intensity, were observed in the high-MVD 18269 and 12424 models, whereas the low-MVD 18254 model showed the least deposition. The SML-PEG deposition also reflected the same trend as f-SSL (Figure 6a). Additionally, the percent area of the tumour section perfused by SML-PEG (Figure S7), that quantifies penetrance, further reflected the trend in SML-PEG deposition. Together, the data suggested that SML-PEG may be used as a surrogate marker for vascular permeability as well as for marking the tumour disposition of therapeutic liposome formulations.

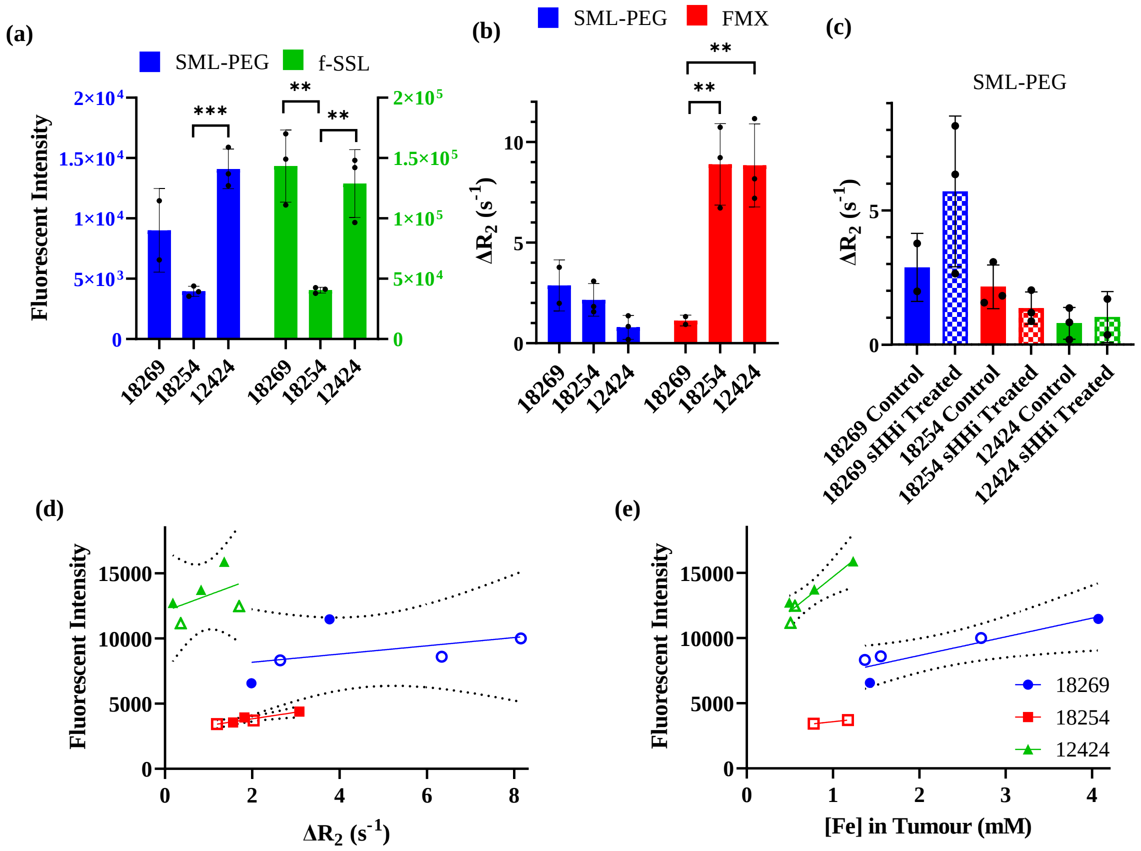

**Figure 6. (a)** Recorded fluorescent intensity of tumour sections (n=3, except SML-PEG treated 18269, where n = 2) for control groups in the 18269, 18254, and 12424 PDX models 24 hours post injection of DiD-DS labelled SML-PEG and f-SSL. **(b)** Recorded $\Delta R_2$ (n = 3, except SML-PEG treated 18269, where n = 2) for control groups in the 18269, 18254, and 12424 PDX models 24 hours after injection of DiD-DS-labelled SML-PEG or FMX at equivalent Fe doses (50 mg/kg). **(c)** Recorded $\Delta R_2$ for control- and sHHi-treated groups in the 18269, 18254, and 12424 PDX models 24 hours post injection of DiD-DS-labelled SML-PEG (n = 3, except for control 18269 and sHHi-pretreated 12424, where n = 2). **(d)** Linear correlation between $\Delta R_2$ and fluorescence intensity of DiD-DS-labelled SML-PEG distribution in control (closed marker) and sHHi-pretreated (open marker) groups in the 18269, 18254, and 12424 PDX models 24 hours post injection. Dashed lines represent the 95% confidence interval. **(e)** Correlation between Fe concentration, as determined by ICP-MS, and fluorescence intensity of DiD-DS-labelled SML-PEG distribution in control (closed marker) and sHHi-pretreated (open marker) groups in the 18269, 18254 and 12424 PDX models 24 hours post injection. Dashed lines represent the 95% confidence interval.

Given that our goal is to determine tumour deposition using non-invasive methods, the MR contrast-enhancement measured by $\Delta R_2$ values in vivo was compared with tissue-level deposition of SML-PEG fluorescence in individual tumours from different PDX models. An additional Ferumoxytol (FMX)-injected control group was introduced, given that FMX is the only clinically-approved iron oxide nanoparticle available, and uncoated SMLs are too unstable and biologically incompatible to be used as controls. The $\Delta R_2$ values invoked by SML-PEG in the different PDX models are shown in Figure 6b, and the highest contrast was generated in the high-MVD PDX #18269, whereas lower contrast was observed in the less permeable PDX #18254 and 12424 models. In contrast however, an equivalent dose of injected FMX generated low $\Delta R_2$ values in the high-MVD PDX #18269 model that had showed high SML-PEG and f-SSL deposition, and higher $\Delta R_2$ values in PDXs #12424 and #18254 models (Figure 6b). Given that the $\Delta R_2$ values generated by SML-PEGs reflected tumour deposition of f-SSL and SML-PEGs more closely than the $\Delta R_2$ values generated by FMX, the SML-PEGs may serve as better surrogates for predicting therapeutic nanoparticle deposition in PDAC PDX tumours than FMX. The SML-PEGs share the outer leaflet composition with f-SSL and clinically approved nanoparticulate therapeutics and therefore may emulate the bio-distribution of the therapeutics.

Vascular permeability may be manipulated in PDAC tumours by treating them with small-molecular weight therapeutics, such as sonic hedgehog signal inhibitors(sHHi), which alter the functional vessel density and vascular morphology to enhance vascular permeability and nanoparticle deposition in tumours. Therefore, we also investigated whether the tumour deposition and contrast generated by SML-PEGs mirrored vascular permeability alterations induced by the sHHi priming (Figure 6c). The sHHi priming was most evident in the 18269 model; #18269 tumours pre-treated with the sHHI showed significantly higher $\Delta R_2$ compared to untreated controls, whereas $\Delta R_2$ showed a decreasing and an increasing trend in sHHi pre-treated #18254 and #12424, respectively. We measured the MR contrast-enhancement generated by SML-PEGs in parallel with their tissue-level deposition; in individual tumours within each PDX group, the tissue-level deposition correlated linearly with both MR contrast-enhancement ($\Delta R_2$) and intratumour Fe concentration determined by ICP-MS (Figure 6d and e), establishing that tumour deposition of SML-PEGs can be predicted by MRI. Even though a larger error was noted in the $\Delta R_2$ measurements than in the ICP-MS data, potentially caused by the lower MRI sensitivity than ICP-MS, the data demonstrates that SML-PEG deposition reflects the subtle but therapeutically relevant permeability alterations induced by sHHi treatment. Therefore, it may be possible to stratify patient tumours prior to chemotherapy-administration based on their relative SML-PEG uptake by MRI that predicts a tumour's propensity to deposit externally similar nanoparticulate drug carriers.

## 4. CONCLUSIONS

We report the development of a two-step method for the preparation of monodisperse, colloidally stable SMLs having selectable colloidal and magnetic properties that can be exploited for numerous applications. SML-PEG, consisting of size-controlled clusters of superparamagnetic iron oxide nanoparticles enveloped within a phospholipid bilayer that can be tuned to resemble diverse lipidic nanoparticle delivery vehicles such as FDA-approved Doxil® and Onivyde®, exhibit (i) extended circulation time; (ii) tumour deposition that is comparable to liposomes of the same composition; (iii) good MRI $T_2$-contrast, and (iv) tumour retention up to 1 week.

Inter-individual variations in SML-PEG deposition were observed in three PDX models that reflect the large patient-to-patient variability observed in PDAC, highlighting the need for a surrogate marker that enables optimisation of treatment- and tumour-priming regimens, and predicts responder patients without subjecting them to the toxicity of chemotherapy. SML-PEG also provided a readout of PDAC responses to tumour priming approaches that increase permeability and perfusion, and enhance deposition of liposome drug carriers at the organ/tissue level (by *in vivo* MRI) and tissue/histological level (by *ex vivo* fluorescence microscopy) that enhance nanoparticle tumour deposition in some patient PDAC isolates but not others.

The findings of these studies highlight the need for clinical optimisation of treatment strategies for this nearly uniformly-lethal disease in order to increase tumour drug delivery and efficacy. SMLs produced by controlled formulation are a step towards non-invasive MRI stratification approaches for patient stratification and selection for potential clinical benefit prior to administration of chemotherapy-loaded nano-liposomal therapeutics.

## AUTHOR INFORMATION

### Corresponding Authors

* Dermot F. Brougham (dermot.brougham@ucd.ie) and Robert M. Straubinger (rms@buffalo.edu)

### Present Address

‡School of Medicine, University of Nottingham, NG7 2RD, UK

### Author Contributions

CM carried out preparation and characterisation of formulation. CM, TRC and JS conducted in vivo studies. CM composed the first draft; CM, TRC, RMS and DFB revised and edited the manuscript. All authors have given approval to the final version of the manuscript.

### Funding Sources

This work was supported by Science Foundation Ireland (under the projects 15/TIDA/2945 and 16/IA/4584) to DB, the U.S. National Inst. of Health/NCI grant R01CA198096 to RMS, and utilised the Translation Imaging Shared Resource of Roswell Park Comprehensive Cancer Center, Buffalo, NY, which receives partial support from NIH Comprehensive Cancer Support grant P30CA016056. CM received support from the Irish Research Council (GOIPG/2015/3492), a Fulbright Commission of Ireland Student Award (2018/2019), a Travel Fellowship from the European Association for Cancer Research, and a Researcher Mobility Grant from the Royal Society of Chemistry.

## ACKNOWLEDGMENTS

We would like to thank David van Acken in the National Centre for Isotope Geochemistry, UCD for ICP analysis, Ninfa Straubinger (UB/SUNY) for technical support for the *in vivo* studies and Steve Turowski (Roswell Park) for assistance with MRI studies.

## DATA AVAILABILITY

The raw/processed data required to reproduce our findings are available from the authors.

## 5. REFERENCES

[1] T.M. Allen, P.R. Cullis, Liposomal Drug Delivery Systems: From Concept to Clinical Applications, Advanced Drug Delivery Rev. 65 (2013) 36 - 48.
[2] B.S. Pattni, V.V. Chupin, V.P. Torchilin, New Developments in Liposomal Drug Delivery, Chem. Rev. 115 (2015) 10938 - 10966.
[3] D.C. Drummond, C.O. Noble, M.E. Hayes, J.W. Park, D.B. Kirpotin, Pharmacokinetics and in vivo Drug Release Rates in Liposomal Nanocarrier Development, J. Pharm. Sci. 97 (2008) 4696 - 4740.
[4] N. Filipczak, J. Pan, S.S.K. Yalamarty, V.P. Torchilin, Recent Advancements in Liposome Technology, Adv. Drug Deliv. Rev. 156 (2020) 4 - 22.
[5] P. Grodzinski, M. Kircher, M. Goldberg, A. Gabizon, Integrating Nanotechnology into Cancer Care, ACS Nano 13 (2019) 7370 - 7376.
[6] G. Gregoriadis, A.T. Florence, Liposomes in Drug Delivery. Clinical, Diagnostic and Ophthalmic Potential, Drugs 45 (1993) 15 - 28.
[7] F.J.T. Fildes, Liposomes: From Physical Structure to Therapeutic Applications, Elsevier/North-Holland Biomedical Press, The Netherlands, 1981.
[8] C. Ross, M. Taylor, N. Fullwood, D. Allsop, Liposome Delivery Systems for the Treatment of Alzheimer's Disease, Int. J. Nanomed. 13 (2018) 8507 - 8522.
[9] A. Gabizon, H. Shmeeda, Y. Barenholz, Pharmacokinetics of PEGylated Liposomal Doxorubicin: Review of Animal and Human Studies, Clin. Pharmacokinet. 42 (2003) 419 - 436.
[10] K.E. Richards, A.E. Zeleniak, M.L. Fishel, J. Wu, L.E. Littlepage, R. Hill, Cancer-associated Fibroblast Exosomes Regulate Survival and Proliferation of Pancreatic Cancer Cells, Oncogene 36 (2017) 1779 - 1778.
[11] S.A. Melo, L.B. Luecke, C. Kahlert, A.F. Fernandez, S.T. Gammon, J. Kaye, V.S. LeBleu, E.A. Mittendorf, J. Weitz, N. Rahbari, C. Reissfelder, C. Pilarsky, M.F. Fraga, D. Piwnica-Worms, R. Kalluri, Glypican-1 Identifies Cancer Exosomes and Detects Early Pancreatic Cancer, Nat. 523 (2015) 177 - 182.
[12] A. Gabizon, R. Shiota, D. Papahadjopolous, Pharmacokinetics and Tissue Distribution of Doxorubicin Encapsulated in Stable Liposomes With Long Circulation Times, J. Nat. Cancer Inst. 81 (1989) 1484 - 1488.
[13] F.M. Muggia, J.D. Hainsworth, S. Jeffers, P. Miller, S. Groshen, M. Tan, L. Roman, B. Uziely, L. Muderspach, A. Garcia, A. Burnett, F.A. Greco, C.P. Morrow, L.J. Paradiso, L.J. Liang, Phase II Study of Liposomal Doxorubicin in Refractory Ovarian Cancer: Antitumor Activity and Toxicity Modification by Liposomal Encapsulation, J. Clin. Oncol. 15 (1997) 987 - 993.
[14] A. Wang-Gillam, R.A. Hubner, J.T. Siveke, D.D. Von Hoff, B. Belanger, F.A. de Jong, B. Mirakhur, L.-T. Chen, NAPOLI-1 Phase 3 Study of Liposomal Irinotecan in Metastatic Pancreatic Cancer: Final Overall Survival Analysis and Characteristics of Long-term Survivors, Eur. J. Cancer 108 (2019) 78 - 87.
[15] D.C. Drummond, C.O. Noble, Z. Guo, K. Hong, J.W. Park, D.B. Kirpotin, Development of a Highly Active Nanoliposomal Irinotecan Using a Novel Intraliposomal Stabilization Strategy, Cancer Res. 66 (2006) 3271 - 3277.
[16] R.K. Ramanathan, R.L. Korn, N. Raghunand, J.C. Sachdev, R.G. Newbold, G. Jameson, G.J. Fetterly, J. Prey, S.G. Klinz, J. Kim, J. Cain, B.S. Hendriks, D.C. Drummond, E. Bayever, J.B. Fitzgerald, Correlation Between Ferumoxytol Uptake in Tumor Lesions by

MRI and Response to Nanoliposomal Irinotecan in Patients with Advanced Solid Tumors: A Pilot Study, Clin. Cancer Res. 23 (2017) 3638 - 3648.

[17] K.P. Olive, M.A. Jacobetz, C.J. Davidson, A. Gopinathan, D. McIntyre, D. Honess, B. Madhu, M.A. Goldgraben, M.E. Caldwell, D. Allard, K.K. Frese, G. DeNicola, C. Feig, C. Combs, S.P. Winter, H. Ireland-Zecchini, S. Reichelt, W.J. Howat, A. Chang, M. Dhara, L. Wang, F. Rueckert, R. Gruetzmann, C. Pilarsky, K. Izeradjene, S.R. Hingorani, P. Huang, S.E. Davies, W. Plunkett, M. Egorin, R.H. Hruban, N. Whitebread, K. McGovern, J. Adams, C. Iacobuzio-Donahue, J. Griffiths, D.A. Tuveson, Inhibition of Hedgehog Signaling Enhances Delivery of Chemotherapy in a Mouse Model of Pancreatic Cancer, Sci. 324 (2009) 1457 - 1461.

[18] T. Roy Chaudhuri, N.L. Straubinger, R.F. Pitoniak, B.L. Hylander, E.A. Repasky, W.W. Ma, R.M. Straubinger, Tumor-Priming Smoothened Inhibitor Enhances Deposition and Efficacy of Cytotoxic Nanoparticles in a Pancreatic Cancer Model, Mol. Cancer Ther. 15 (2016) 84 - 93.

[19] J. Wang, D.K.W. Chan, A. Sen, W.W. Ma, R.M. Straubinger, Tumor Priming by SMO Inhibition Enhances Antibody Delivery and Efficacy in a Pancreatic Ductal Adenocarcinoma Model, Mol. Cancer Ther. 18 (2019) 2074 - 2084.

[20] M. De Cuyper, M. Joniau, Magnetoliposomes: Formation and Structural Characterization, Eur. Biophys. J. 15 (1988) 311 - 319.

[21] G. Bealle, R. Di Corato, J. Kolosnjaj-Tabi, V. Dupuis, O. Clement, F. Gazeau, C. Wilhelm, C. Menager, Ultra Magnetic Liposomes for MR Imaging, Targeting, and Hyperthermia, Langmuir 28(32) (2012) 11843-11851.

[22] M.-S. Martina, J.-P. Fortin, C. Menager, O. Clement, G. Barratt, G.-M. Cecile, F. Gazeau, V. Cabuil, S. Lesieur, Generation of Superparamagnetic Liposomes Revealed as Highly Efficient MRI Contrast Agents for in vivo Imaging, JACS 127 (2005) 10676 - 10685.

[23] C. Riviere, M.-S. Martina, Y. Tomita, C. Wilhelm, A. Tran Dinh, C. Menager, E. Pinard, S. Lesieur, F. Gazeau, S. Jacques, Magnetic Targeting of Nanometric Magnetic Fluid Loaded Liposomes to Specific Brain Intravascular Areas: A Dynamic Imaging Study in Mice, Radiol. 244 (2007) 439 - 448.

[24] M. Dai, C. Wu, H.-M. Fang, L. Li, J.-B. Yan, D.-L. Zeng, T. Zou, Thermo-responsive Magnetic Liposomes for Hyperthermia-triggered Local Drug Delivery, J. Microencap. 34 (2017) 408 - 415.

[25] C.J. Meledandri, T. Ninjbadgar, D.F. Brougham, Size-controlled Magnetoliposomes with Tunable Magnetic Resonance Relaxation Enhancements, J. Mater. Chem. 21 (2011) 214 - 222.

[26] N. Pinna, S. Grancharov, P. Beato, P. Bonville, M. Antonietti, M. Niederberger, Magnetite Nanocrystals: Nonaqueous Synthesis, Characterization, and Solubility, Chem. Mater. 17 (2005) 3044 - 3049.

[27] F. Bray, J. Ferlay, I. Soerjomataram, R.L. Siegel, L.A. Torre, A. Jemal, Global Cancer Statistics 2018: GLOBOCAN Estimates of Incidence and Mortality Worldwide for 36 Cancers in 185 Countries, CA: Cancer J. Clin. 68 (2018) 394 - 424.

[28] Pancreatic Cancer, About the Pancreas - Prognosis. (Accessed 12/10 2020).

[29] R.L. Siegel, K.D. Miller, A. Jemal, Cancer Statistics, 2020, CA: Cancer J. Clin. 70 (2020).

[30] O. Coleman, M. Henry, F. O'Neill, S. Roche, N. Swan, L. Boyle, J. Murphy, J. Meiller, N.T. Conlon, J. Geoghegan, K.C. Conlon, V. Lynch, N.L. Straubinger, R.M. Straubinger, G. McVey, M. Moriarty, P. Meleady, M. Clynes, A Comparative Quantitative LC-MS/MS Profiling Analysis of Human Pancreatic Adenocarcinoma, Adjacent-normal Tissue, and Patient-derived Tumour Xenografts, Proteomes 6 (2018) 45 - 65.

[31] M.W. Muller, H. Friess, J. Koninger, D. Martin, M.N. Wente, U. Hinz, G.O. Ceyhan, P. Blaha, J. Kleeff, M.W. Buchler, Factors Influencing Survival After Bypass Procedures in Patients with Advanced Pancreatic Adenocarcinomas, Am. J. Surg. 195 (2008) 221 - 228.
[32] M. Hidalgo, Pancreatic Cancer, N. Engl. J. Med 362 (2010) 1605 - 1617.
[33] P. Vincent, S. Vaibhav, S. Diane, R.L. Caio, O. Allyson, P. Philip, S. Wasif, K. Aparna, O. Michael, S.L. Jack, L. Chrystal, A phase 1/2 study of metronomic 5-fluorouracil (5-FU) plus nabpaclitaxel, bevacizumab, leucovorin, and oxaliplatin (FABLOx) in patients with metastatic pancreatic cancer, Ann Oncol 28 (2017).
[34] X.-J. Liang, C. Chen, Y. Zhao, P.C. Wang, Circumventing Tumor Resistance to Chemotherapy by Nanotechnology, Methods in Mol. Biol. 596 (2010) 467 - 488.
[35] J.E. Faris, L.S. Blaszkowsky, S. McDermott, A.R. Guimaraes, J. Szymonifka, M.A. Huynh, C.R. Ferrone, J.A. Wargo, J.N. Allen, L.E. Dias, E.L. Kwak, K.D. Lillemoe, S.P. Thayer, J.E. Murphy, A.X. Zhu, D.V. Sahani, J.Y. Wo, J.W. Clark, C. Fernandez-Del Castillo, D.P. Ryan, T.S. Hong, FOLFIRINOX in Locally Advanced Pancreatic Cancer: The Massachusetts General Hospital Cancer Center Experience, The Oncologist 18 (2013) 543 - 548.
[36] M. Bashir , R., L. Bhatti , D. Marin , R.C. Nelson, Emerging Applications for Ferumoxytol as a Contrast Agent in MRI, J. Magn. Res. Imag. 41 (2015) 884 - 898.
[37] E.D. Lehrman, A.N. Plotnik, T. Hope, D. Saloner, Ferumoxytol-enhanced MRI in the Peripheral Vasculature, Clin. Radiol. 74 (2019) 37 - 50.
[38] M. Lu, M.H. Cohen, D. Rieves, P. Richard, FDA Report: Ferumoxytol for Intravenous Iron Therapy in Adult Patients with Chronic Kidney Disease, Am. J. Hema. 85 (2010) 315 - 319.
[39] Rienso: Application for New Indication Withdrawn, Reactions Weekly 1542 (2015).
[40] E.K. Fox, F. El Haddassi, J. Hierrezuelo, T. Ninjbadgar, J.K. Stolarczyk, J. Merlin, D.F. Brougham, Size-Controlled Nanoparticle Assembly: Size-Controlled Nanoparticle Clusters of Narrow Size-Polydispersity Formed Using Multiple Particle Types Through Competitive Stabilizer Desorption to a Liquid–Liquid Interface, Small 14 (2018) 1802278 - 1802284.
[41] E. Fox, The Preparation and Characterisation of Stable Colloids of Magnetic Nanoparticles and Nanoparticle Assemblies with Controlled Size and Magnetic Properties, School of Chemistry, Dublin City University, 2013.
[42] J. Pan, F.A. Heberle, S. Tristam-Nagle, M. Szymanski, M. Koepfinger, J. Katsaras, N. Kucerka, Molecular Structures of Fluid Phase Phosphatidylglycerol Bilayers as Determined by Small Angle Neutron and X-ray Scattering, Biochim. Biophys. Acta 1818 (2012) 2135 - 2148.
[43] R. Kimmich, Field-cycling NMR Relaxometry Instrumentation, Model Theories and Applications Preface, New Dev Nmr 18 (2019) V-Vi.
[44] C.J. Meledandri, D.F. Brougham, Low field magnetic resonance techniques in the development of nanomaterials for biomedical applications, Anal Methods-Uk 4(2) (2012) 331-341.
[45] P. Schmitt, M.A. Griswold, P.M. Jakob, M. Kotas, V. Gulani, M. Flentje, A. Haase, Inversion Recovery TrueFISP: Quantification of T(1), T(2), and Spin Density, Magn. Res. in Med. 51 (2004) 661 - 667.
[46] P. Meers, S. Ali, R. Erukulla, A.S. Janoff, Novel Inner Monolayer Fusion Assays Reveal Differential Monolayer Mixing Associated with Cation-dependent Membrane Fusion, Biochim. Biophys. Acta. 1467 (2000) 227 - 243.
[47] B.L. Hylander, R. Pitoniak, R.B. Penetrante, J.F. Gibbs, D. Oktay, J. Cheng, E.A. Repasky, The Anti-tumor Effect of Apo2L/TRAIL on Patient Pancreatic Adenocarcinomas Grown as Xenografts in SCID Mice, J. Trans. Med. 3 (2005) 22 - 35.

[48] J. Schindelin, I. Arganda-Carreras, E. Frise, V. Kaynig, M. Longair, T. Pietzsch, S. Preibisch, C. Rueden, S. Saalfeld, B. Schmid, J.-Y. Tinevez, D.J. White, V. Hartenstein, K. Eliceiri, P. Tomancak, A. Cardona, Fiji: An Open-Source Platform for Biological-Image Analysis, Nat. Methods 9 (2012) 676 - 682.
[49] C.A. Schneider, W.S. Rasband, K.W. Eliceiri, NIH Image to ImageJ: 25 Years of Image Analysis, Nat. Methods 9 (2012) 671 - 675.
[50] C. NDong, J.A. Tate, W.C. Kett, J. Batra, E. Demidenko, L.D. Lewis, H.P. Jack, T.U. Gerngross, K.E. Griswold, Tumor Cell Targeting by Iron Oxide Nanoparticles is Dominated by Different Factors in vitro Versus in vivo, PLoS One 10 (2015) e0115636.
[51] ISO, ISO 22412:2017 Particle size analysis — Dynamic light scattering (DLS), 2017.
[52] C.N. Banwell, Fundamentals for Molecular Spectroscopy, 2nd ed., McGraw-Hill Book Company, London, UK, 1972.
[53] D.L. Huber, Synthesis, properties, and applications of iron nanoparticles, Small 1(5) (2005) 482-501.
[54] M.C. Johnston, J.A. Nicoll, K.M. Redmond, P. Smyth, M.K. Greene, W.J. McDaid, D.K.W. Chan, N.T. Crawford, K.J. Stott, J.P. Fox, N.L. Straubinger, S. Roche, M. Clynes, R.M. Straubinger, D.B. Longley, C.J. Scott, DR5-targeted, Chemotherapeutic Drug-loaded Nanoparticles Induce Apoptosis and Tumor Regression in Pancreatic Cancer i*n vivo* Models, J. Cont. Rel. 324 (2020) 610 - 619.
[55] Z. Varga, J. Mihály , S. Berenyi, A. Bóta, Structural Characterization of the Poly(ethylene glycol) Layer of Sterically Stabilized Liposomes by Means of FTIR Spectroscopy, Eur. Polym. J. 49 (2013) 2415 - 2421.
[56] W.I. Choi, A. Sahu, F.R. Wurm, S.M. Jo, Magnetoliposomes with size controllable insertion of magnetic nanoparticles for efficient targeting of cancer cells, Rsc Adv 9(26) (2019) 15053-15060.
[57] C.J. Meledandri, NMR Studies of Membrane-Bound Nanoparticles and Nanoparticle Assemblies, Dublin City University, 2008.
[58] M.S. Martina, J.P. Fortin, C. Menager, O. Clement, G. Barratt, C. Grabielle-Madelmont, F. Gazeau, V. Cabuil, S. Lesieur, Generation of superparamagnetic liposomes revealed as highly efficient MRI contrast agents for in vivo imaging, Journal of the American Chemical Society 127(30) (2005) 10676-10685.
[59] R. Sabate, R. Barnadas-Rodriguez, J. Callejas-Fernandez, R. Hidalgo-Alvarez, J. Estelrich, Preparation and characterization of extruded magnetoliposomes, International Journal of Pharmaceutics 347(1-2) (2008) 156-162.
[60] A. Gharib, Z. Faezizadeh, S.A.R. Mesbah-Namin, R. Saravani, Preparation, characterization and in vitro efficacy of magnetic nanoliposomes containing the artemisinin and transferrin, Daru 22 (2014).
[61] J.P. Fortin-Ripoche, M.S. Martina, F. Gazeau, C. Menager, C. Wilhelm, J.C. Bacri, S. Lesieur, O. Clement, Magnetic targeting of magnetoliposomes to solid tumors with MR imaging monitoring in mice: Feasibility, Radiology 239(2) (2006) 415-424.
[62] J.K. Stolarczyk, C.J. Meledandri, S.P. Clarke, D.F. Brougham, Size Selectable Nanoparticle Assemblies with Magnetic Anisotropy Tunable Across the Superparamagnetic to Ferromagnetic Range, Chem. Comm. 52 (2016) 13337 - 13340.
[63] L. Xiao, J. Li, D.F. Brougham, E.K. Fox, N. Feliu, A. Bushmelev, A. Schmidt, N. Mertens, F. Kiessling, M. Valldor, B. Fadeel, S. Mathur, Water-Soluble Superparamagnetic Magnetite Nanoparticles with Biocompatible Coating for Enhanced Magnetic Resonance Imaging, ACS Nano 5 (2011) 6315 - 6324.
[64] A. Roch, R.N. Muller, P. Gillis, Theory of proton relaxation induced by superparamagnetic particles, J Chem Phys 110 (1999) 5403 - 5411.

[65] C.J. Meledandri, J.K. Stolarczyk, S. Ghosh, D.F. Brougham, Nonaqueous Magnetic Nanoparticle Suspensions with Controlled Particle Size and Nuclear Magnetic Resonance Properties, Lang. 24 (2008) 14159 - 14165.
[66] A. Gabizon, R. Catane, B. Uziely, B. Kaufman, T. Safra, R. Cohen, F. Martin, A. Huang, Y. Barenholz, Prolonged Circulation Time and Enhanced Accumulation in Malignant Exudates of Doxorubicin Encapsulated in Polyethylene-glycol Coated Liposomes, Cancer Res. 54 (1994) 987 - 992.
[67] R. Toy, E. Hayden, C. Shoup, H. Baskaran, E. Karathanasis, The Effects of Particle Size, Density and Shape on Margination of Nanoparticles in Microcirculation, Nanotech. 22 (2011) 115101 - 115109.
[68] K. Walter, N. Omura, S.-M. Hong, M. Griffith, A. Vincent, M. Borges, M. Goggins, Overexpression of Smoothened Activates the Sonic Hedgehog Signaling Pathway in Pancreatic Cancer-Associated Fibroblasts, Clin. Cancer Res. 6 (2010) 1781 - 1789.
[69] D.V.T. Catenacci, M.R. Junttila, T. Karrison, N. Bahary, M.N. Horiba, S.R. Nattam, R. Marsh, J. Wallace, M. Kozloff, L. Rajdev, D. Cohen, J. Wade, B. Sleckman, H.J. Lenz, P. Stiff, P. Kumar, P. Xu, L. Henderson, N. Takebe, R. Salgia, X. Wang, W.M. Stadler, F.J. de Sauvage, H.L. Kindler, Randomized Phase Ib/II Study of Gemcitabine Plus Placebo or Vismodegib, a Hedgehog Pathway Inhibitor, in Patients With Metastatic Pancreatic Cancer, J Clin Oncol 33(36) (2015) 4284-+.
[70] A.H. Ko, N. LoConte, M.A. Tempero, E.J. Walker, R.K. Kelley, S. Lewis, W.C. Chang, E. Kantoff, M.W. Vannier, D.V. Catenacci, A.P. Venook, H.L. Kindler, A Phase I Study of FOLFIRINOX Plus IPI-926, a Hedgehog Pathway Inhibitor, for Advanced Pancreatic Adenocarcinoma, Pancreas 45(3) (2016) 370-375.
[71] E.U. Saritas, P.W. Goodwill, L.R. Croft, J.J. Konkle, K. Lu, B. Zheng, S.M. Conolly, Magnetic particle imaging (MPI) for NMR and MRI researchers, J Magn Reson 229 (2013) 116-26.
[72] X.Y.Y. Zhou, Z.W. Tay, P. Chandrasekharan, E.Y. Yu, D.W. Hensley, R. Orendorff, K.E. Jeffris, D. Mai, B. Zheng, P.W. Goodwill, S.M. Conolly, Magnetic particle imaging for radiation-free, sensitive and high-contrast vascular imaging and cell tracking, Curr Opin Chem Biol 45 (2018) 131-138.
[73] R. Hachani, M. Lowdell, M. Birchall, N.T.K. Thanh, Tracking stem cells in tissue-engineered organs using magnetic nanoparticles, Nanoscale 5(23) (2013) 11362-11373.
[74] M.K. Greene, T. Chen, E. Robinson, N.L. Straubinger, C. Minx, D.K.W. Chan, J. Wang, J.F. Burrows, S. Van Schaeybroeck, J.R. Baker, S. Caddick, D.B. Longley, D.E. Mager, R.M. Straubinger, V. Chudasama, C.J. Scott, Controlled coupling of an ultrapotent auristatin warhead to cetuximab yields a next-generation antibody-drug conjugate for EGFR-targeted therapy of KRAS mutant pancreatic cancer, Br J Cancer 123(10) (2020) 1502-1512.
[75] B.L. Hylander, N. Punt, H. Tang, J. Hillman, M. Vaughan, W. Bshara, R. Pitoniak, E.A. Repasky, Origin of the vasculature supporting growth of primary patient tumor xenografts, J Transl Med 11 (2013) 110.
[76] R. Sharma, S. Buitrago, R. Pitoniak, J.F. Gibbs, L. Curtin, M. Seshadri, E.A. Repasky, B.L. Hylander, Influence of the implantation site on the sensitivity of patient pancreatic tumor xenografts to Apo2L/TRAIL therapy, Pancreas 43(2) (2014) 298-305.